



<http://www.diva-portal.org>

Postprint

This is the accepted version of a paper published in *IEEE Transactions on Terahertz Science and Technology*. This paper has been peer-reviewed but does not include the final publisher proof-corrections or journal pagination.

Citation for the original published paper (version of record):

Karimi, A., Shah, U., Yu, S., Oberhammer, J. (2024)  
A High-Performance 220–290 GHz Micromachined Waveguide Switch Based on  
Interference Between MEMS Reconfigurable Surfaces  
*IEEE Transactions on Terahertz Science and Technology*, 14(2): 188-198  
<https://doi.org/10.1109/tthz.2024.3356184>

Access to the published version may require subscription.

N.B. When citing this work, cite the original published paper.

Permanent link to this version:

<http://urn.kb.se/resolve?urn=urn:nbn:se:kth:diva-344391>

# A High-Performance 220-290 GHz Micromachined-Waveguide Switch Based on Interference Between MEMS Reconfigurable Surfaces

Armin Karimi, *Student Member, IEEE*, Umer Shah, *senior Member, IEEE*,  
Suxian Yu, *Student Member, IEEE*, Joachim Oberhammer, *fellow Member, IEEE*

**Abstract** — This paper presents a highly-integrated novel silicon micromachined single-pole-single-throw waveguide switch based on two microelectromechanically reconfigurable switching surfaces (MEMS-RSs), which allows optimizing the switching performance by tuning the interference between the two such MEMS-RSs utilizing integrated electrostatic comb-drive actuators. The switch prototype is implemented with axially aligned standard WR-3.4 waveguide ports with a total footprint of 3mm×3.5mm×1.2mm. The measured blocking (OFF) state insertion loss (isolation) and return loss, measured between two standard WR-3.4 waveguide flanges, are 28.5-32.5 dB and better than 0.7 dB, and the propagating (ON) state insertion and return losses are 0.7-1.2 dB and better than 17 dB in the 220-290 GHz frequency band, respectively. The measured results were in excellent agreement with the simulation data, implying 27.5% fractional bandwidth, which is very close to a full waveguide band performance. For further investigations, two variants of the switching circuit with only a single MEMS-RS and without any MEMS-RSs have also been fabricated. The single MEMS-RS switch achieved the OFF-state isolation, ON-state insertion loss, and return loss of only 11.5-12.5 dB, 0.8-1.3 dB, and better than 12 dB from 220 to 274 GHz, respectively, which clearly indicates the drastic performance improvement of the interference-based double MEMS-RSs switch design. Moreover, measurement of the waveguide-only reference structure showed that the waveguide section alone, attributed to 0.2-0.5 dB of the measured ON-state insertion loss of the double MEMS-RSs switch, and the rest is due to the introduction of the MEMS-RSs inside the waveguides.

**Index Terms** — MEMS, micromachined waveguide, reconfigurable surface, rectangular waveguide, SOI wafer, SPST switch, switch, silicon micromachining, millimeter-wave, sub-terahertz, waveguide switch.

This Manuscript received xxxxx xx, 2023; accepted xxxxx xx, 2023. Date of publication xxxxx xx, 2023; date of current version xxxxx xx, 2023. The contribution of KTH was funded in part by CAR2TERA project and the CAR2TERA project itself has received funding from the European Union's Horizon 2020 research and innovation program under grant agreement No 824962, and in part by the Swedish Foundation for Strategic Research under grant agreement CHI19-0027, and in part by Marie Skłodowska-Curie Grant agreement 811232. (*Corresponding author: Armin Karimi*).

A. Karimi, U. Shah, S. Yu, and J. Oberhammer are with the Micro and Nanosystems Technology Division, School of Electrical Engineering and Computer Science, KTH Royal Institute of Technology, Stockholm SE-100 44, Sweden. ([arminka@kth.se](mailto:arminka@kth.se), [umers@kth.se](mailto:umers@kth.se), [suxian@kth.se](mailto:suxian@kth.se), [joachim@kth.se](mailto:joachim@kth.se))

Color versions of one or more of the figures in this article are available online at <http://ieeexplore.ieee.org>

Digital Object Identifier xxxxxxxxxxxxxxxxxxxxxx

## I. INTRODUCTION

THERE has been a growing interest in the millimeter-wave (mm-wave) and sub-terahertz (sub-THz) spectrum in recent years due to emerging applications in short-range radars, high data-rate communication systems, and sensors, as higher resolutions and broader bandwidths can be achieved at higher frequency bands. Moreover, the space industry has increasingly focused on mm-wave and sub-THz frequency ranges to develop lightweight and compact systems for environmental sensing applications.

Silicon micromachining is a compelling fabrication technology that facilitates integrating waveguide circuits at mm-wave and sub-THz frequencies. It is very well suited for implementing highly accurate, micrometer-size lithographically-defined features and allows integrating active and passive components onto a single chip, resulting in very compact systems [1]. Silicon-micromachined devices are volume manufacturable with high product uniformity and very low loss due to surface roughness down to a few nanometers. Deep reactive ion etching (DRIE) and sidewall metallization are commonly used in silicon micromachining to realize hollow waveguides, which are preferred over planar transmission lines at sub-THz frequencies due to low insertion loss and high power handling capability. The lowest insertion loss for hollow rectangular waveguides is reported to be 0.02-0.07 and 0.05-0.1 dB/mm for WR-3.4 [2] and WR-1.5 silicon micromachined waveguides [3], [4], respectively, and micromachined waveguides operating up to 2.7 THz have also been demonstrated in [5].

Switches are essential components for reconfigurable circuits. The most basic switching elements are single-pole-single-throw (SPST) switches, which can be utilized as building blocks to implement more complex switching circuits, such as multi-pole-multi-throw and crossover switches. Conventional mechanical waveguide switches, though achieving excellent RF performance, are based on macro-scale mechanics requiring a waveguide section to be moved or rotated by a motor [6]–[10], and thus are bulky, heavy, slow, have high power consumption, and cannot achieve a high integration density in waveguide circuits. For instance, despite the single-pole-double-throw (SPDT) waveguide switch recently presented by JPL in [10] has achieved exceptional isolation of better than 75 dB, excellent insertion and return losses of better than 0.6 and 20 dB in the 250-310 GHz frequency band, it has a very slow switching speed and a very high power consumption.

> REPLACE THIS LINE WITH YOUR MANUSCRIPT ID NUMBER (DOUBLE-CLICK HERE TO EDIT) <

Alternatively, silicon micromachining allows the integration of microelectromechanical (MEMS) actuators with different waveguide components. Thus, several MEMS waveguide switches fabricated by silicon micromachining have been shown in [11]–[19]. These rectangular waveguide-based MEMS switches are widely used in high-frequency systems and offer low insertion loss, high isolation, high linearity, large operation bandwidth, low power consumption, microsecond-range switching speed, and high miniaturization. In addition to switches, a large range of further silicon micromachined devices operating at sub-THz and THz frequencies have been demonstrated, such as phase shifters [20], orthogonal mode transducers (OMTs) [21], antennas [22], and filters [23].

The authors have previously demonstrated an SPST switch, operating based on a single microelectromechanically reconfigurable switching surface (MEMS-RS), implemented for the 60-70 and the 500-750 GHz frequency bands [14], [24]. Isolation, insertion, and return losses of 19-24 dB, 2.5-3 dB, and 6-8 dB, respectively, were reported for the SPST switch operating at 500-750 GHz [14]. However, many applications, particularly radiometers, require significantly better RF performance. Although cascading multiple instances of such SPST switches in series improves the isolation of the resulting SPST switch, the performance of the cascaded device may not satisfy the performance requirements needed for designing more complex switching circuits, as cascading does not necessarily improve the insertion and return losses. Instead, using two sets of MEMS-RSs and tuning the interference between them, utilizing integrated MEMS actuators, results in an excellent improvement in the RF performance, which is experimentally verified and presented for the first time in this paper.

The proposed SPST switch in this paper utilizes two sets of MEMS-RSs, resulting in a drastic improvement in all three SPST switch's performance criteria (isolation, insertion loss, and return loss) by interference effect while maintaining almost full waveguide bandwidth. The implemented switch prototype features axial standard WR-3.4 waveguide interfaces for easy integration in conventional rectangular waveguide-based systems without requiring additional transition to maintain a compact footprint. The performance improvement of the proposed double MEMS-RSs SPST switch is demonstrated by comparing it to a single MEMS-RS SPST switch and a waveguide-only reference structure, which are also fabricated with the proposed switch design on the same mask-set. Moreover, the tunable nature of the MEMS-RSs enables the mitigation of fabrication tolerances, leading to the development of a robust SPST switch design.

## II. CONCEPT AND DESIGN

Fig. 1a shows an overview of the proposed single-pole-single-throw (SPST) switch, which consists of two microelectromechanically reconfigurable switching surfaces (MEMS-RSs), two single-stepped  $E$ -plane bends at the switching junction, and two  $E$ -plane transitions at the input/output ports [25], all integrated on a single silicon-micromachined chip, resulting in a very compact,

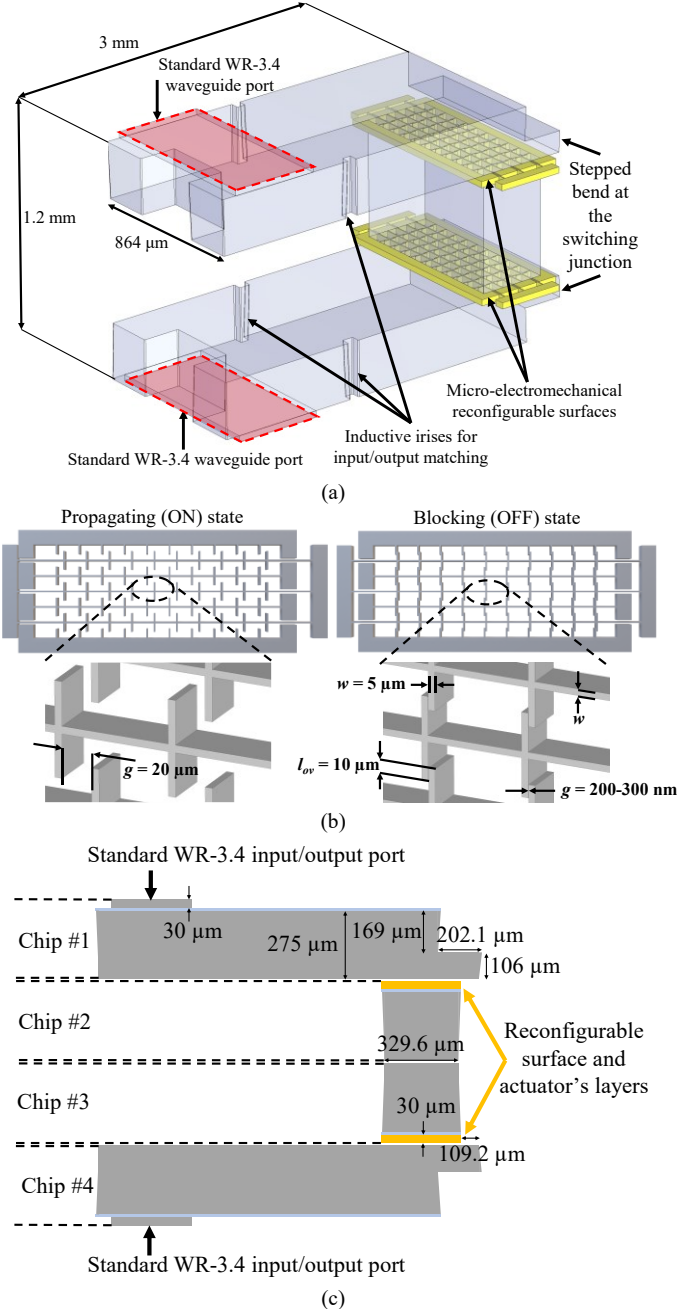


Fig. 1. (a) Overview of the proposed double microelectromechanically reconfigurable switching surfaces single-pole-single-throw switch; (b) configuration of the reconfigurable switching surfaces in the propagating and blocking states, consisting of five  $H$ -plane and ten  $E$ -plane cantilever rows ( $g$ : gap between the switching cantilevers,  $l_{ov}$ : overlap of the switching cantilevers at the contact area); (c) cross-section view of the designed SPST switch with axial standard WR-3.4 waveguide ports and detailed dimensions.

$3\text{mm} \times 3.5\text{mm} \times 1.2\text{mm}$ -large, device. The switch operates based on short-circuiting the dominant mode of rectangular waveguide ( $\text{TE}_{10}$ ) in the blocking (OFF) state while minimally interfering with the wave propagation in the propagating (ON) state [14]. The ON-OFF switching mechanism is implemented by the MEMS-RSs, which are controlled by electrostatic comb-drive MEMS actuators. Fig. 1b depicts the configuration of the MEMS-RSs in the propagating and blocking states. A large number of  $E$ -plane cantilevers increases the OFF-state isolation ( $ISO$ ) and negatively influences the ON-state return

> REPLACE THIS LINE WITH YOUR MANUSCRIPT ID NUMBER (DOUBLE-CLICK HERE TO EDIT) <

loss ( $RL$ ) and insertion loss ( $IL$ ). However, a large number of  $H$ -plane cantilevers leads to better ON-state  $RL$  and  $IL$  and deteriorates the OFF-state  $ISO$  [14]. Considering this trade-off and the comprehensive parameter study performed in [14], the MEMS-RSs include five  $H$ -plane and ten  $E$ -plane cantilever rows, resulting in 60 contact points with  $10\mu\text{m}$  of overlap ( $l_{ov}$ ) between the switching cantilevers at the contact area. The MEMS-RSs consist of two sets of switching cantilevers; the first set is fixed, and the second set is suspended and moves in the lateral direction. When the switch is in the propagating state, there is a  $20\mu\text{m}$  gap between the fixed and suspended cantilevers, which allows the wave to propagate through the MEMS-RSs. However, when the switch is in the blocking state, the suspended cantilevers move toward the fixed ones and block the wave propagation.

The proposed SPST switch geometry is implemented by two sequential MEMS-RSs, which are controlled by comb-drive MEMS actuators. There are two reasons for having two sequential MEMS-RSs in each SPST switch:

- 1) Any reflected power from the MEMS-RSs in the ON state is problematic and degrades the return loss of the switch. Thus, the return loss of the switch ( $|S_{11}|$  in the ON state) is minimized by two sequential MEMS-RSs in the waveguide path, which are designed for destructive interference at the input port in the frequency band of interest.
- 2) Utilizing two sequential MEMS-RSs instead of only one MEMS-RS, as presented in [14], in the signal path doubles the isolation of the switch ( $|S_{21}|$  in the OFF state).

However, as the distance between the MEMS-RSs is fixed and imposed by the thickness of the utilized silicon-on-insulator (SOI) wafer, the width of the out-of-plane waveguide section ( $329.6\mu\text{m}$ ) and the offset of the out-of-plane waveguide from the end-wall ( $109.2\mu\text{m}$ ) are optimized to tune this interference (shown in Fig. 1c). The MEMS-RSs are designed to interfere minimally with the wave propagation in the ON state, with the contact gap ( $g$ ) of  $20\mu\text{m}$ , to enhance the return loss and insertion loss. On the other hand, the switching cantilevers are designed not to rely on electrical contact between the many contact points in the OFF state and are optimized to achieve its OFF state performance even in capacitive contact mode with a contact gap ( $g$ ) of up to  $300\text{nm}$ .

The switch is designed to be fabricated by silicon-micromachining on four layers of SOI chips, consisting of a handle layer ( $275\mu\text{m}$ ), which defines the micromachined waveguide height, a device layer ( $30\mu\text{m}$ ), and a buried oxide layer ( $3\mu\text{m}$ ). Fig. 1c shows a cross-section view of the switching circuit with detailed dimensions of the designed switch. The waveguides are etched on the handle layer, and the MEMS-RSs with their electrostatic actuators are etched on the device layer. The MEMS-RSs, implemented in the device layer, are in-plane (parallel) with the wafer surface. However, they must be oriented perpendicular to the wave propagation direction, which is also in-plane with the wafer surface in a typical micromachined waveguide system. Therefore, the two MEMS-RSs are positioned at the vertical (out-of-plane)

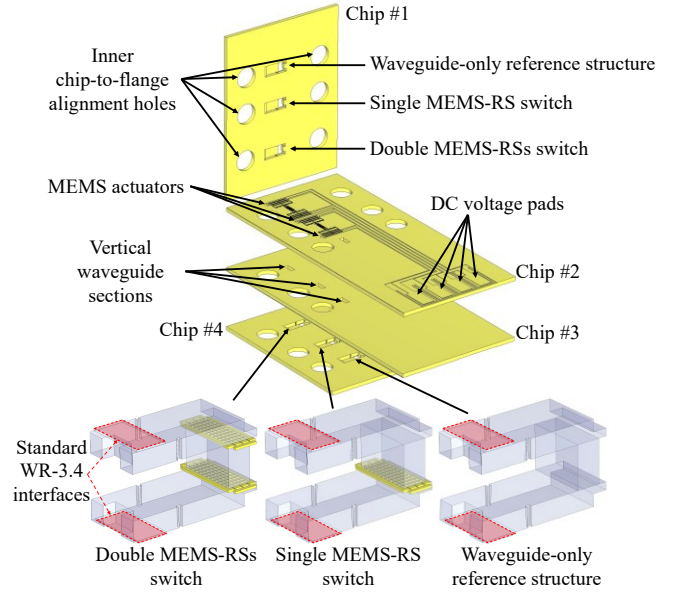


Fig. 2. Overview of the vertically stacked chips. The reduced-height in-plane waveguides and ports are etched in chips #1 and #4, and the reconfigurable switching surfaces and electrostatic actuators are etched in chips #2 and #3. Each prototype contains three devices, including a single and a double microelectromechanically reconfigurable switching surfaces switches and a waveguide-only reference structure.

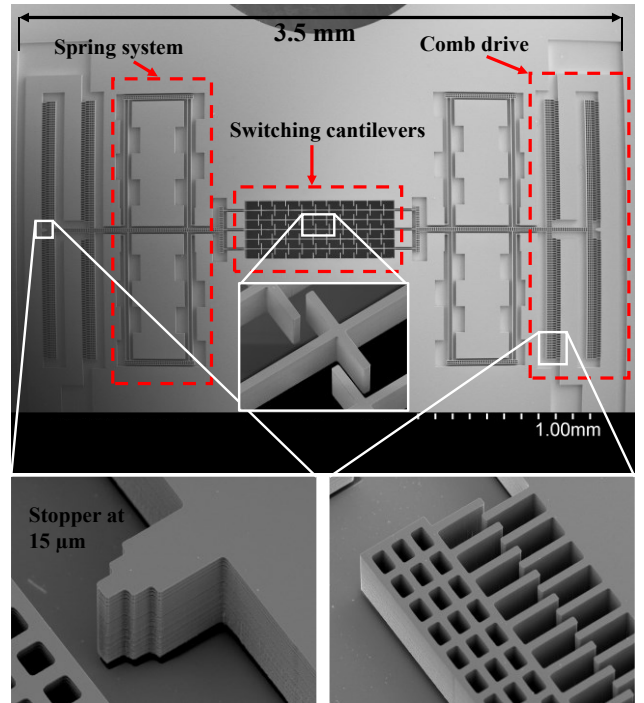


Fig. 3. Scanning electron microscope (SEM) image of the microelectromechanically reconfigurable switching surface and the electrostatic MEMS actuator, etched on the device layer of the SOI chips #2 and #3, with zoomed-in views on the switching cantilevers, stopping mechanism at the distance of  $15\mu\text{m}$ , and comb-fingers.

waveguide section and sandwiched between two in-plane micromachined waveguides, which necessitates utilizing two stepped  $E$ -plane bends at the switching junction for coupling the waves from/to the in-plane waveguides to/from the out-of-plane waveguides (as shown in Fig. 1c). Furthermore, to be

> REPLACE THIS LINE WITH YOUR MANUSCRIPT ID NUMBER (DOUBLE-CLICK HERE TO EDIT) <

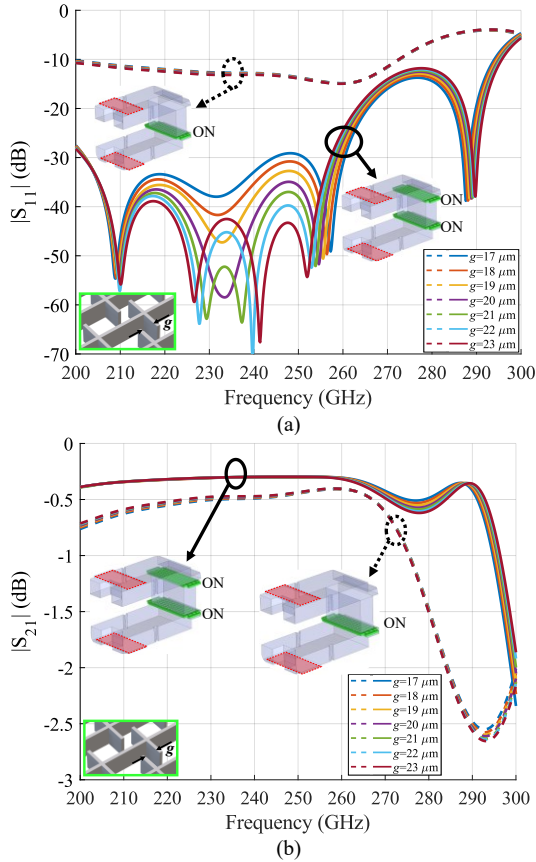


Fig. 4. Simulated (a)  $S_{11}$  and (b)  $S_{21}$  of the single (dashed) and double (solid) MEMS-RSs switches with different contact gaps in the propagating state.

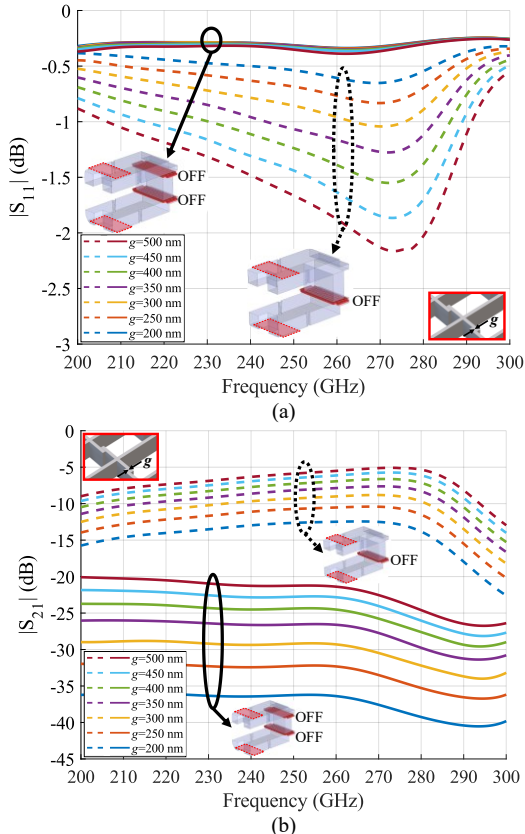


Fig. 5. Simulated (a)  $S_{11}$  and (b)  $S_{21}$  of the single (dashed) and double (solid) MEMS-RSs switches with different contact gaps in the blocking state.

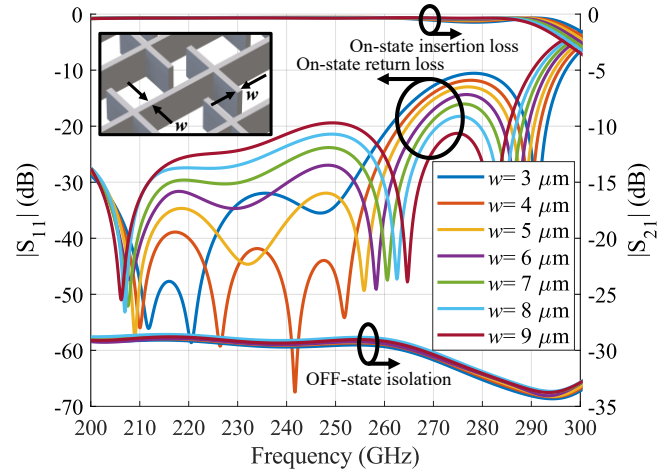


Fig. 6. Influence of the switching cantilever's width ( $w = \{3,4,5,6,7,8,9\}$ ) on the ON (when  $g = 20\mu\text{m}$ ) and OFF (when  $g = 300\text{nm}$ ) states performance of the double microelectromechanically reconfigurable switching surfaces switch.

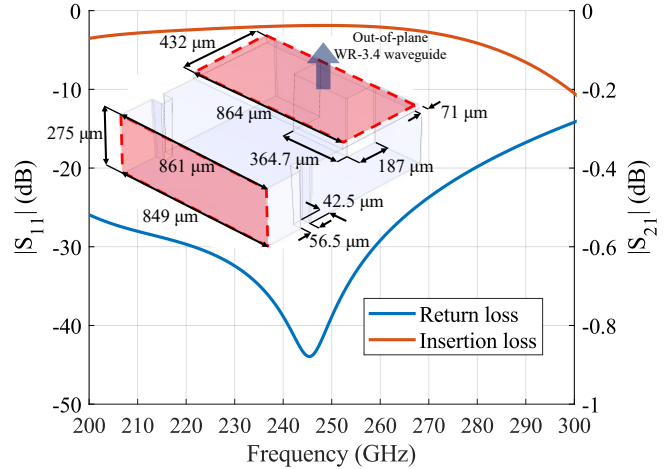


Fig. 7. Simulated insertion and return losses of the stepless  $E$ -plane transition from reduced-height ( $275\mu\text{m}$ ) in-plane waveguides to standard WR-3.4 waveguide, utilized for the input/output interfaces, with detailed dimensions.

able to characterize the designed switch, the test ports have to be routed to the device surface, which requires two further  $E$ -plane transitions from the reduced-height in-plane waveguides to standard WR-3.4 waveguide ports. These transitions, utilized for the device interface, are designed without any  $E$ -plane step in the waveguide's longitudinal cross-section [25], as the fabrication process only permits stepped geometries with steps towards the device layer of the SOI wafer.

In addition to the double MEMS-RSs SPST switch, the fabricated prototype consists of a single MEMS-RS SPST switch and a waveguide-only reference structure on the same chips so that all the variants are fabricated simultaneously and undergo the same fabrication conditions, leading to a more credible comparison between the  $S$ -parameters of different variants. Fig. 2 shows an overview of the vertically stacked chips. While the two middle chips (chips #2 and #3) contain the MEMS-RSs and electrostatic MEMS actuators, the topmost (chip #1) and bottommost (chip #4) chips contain the in-plane waveguides (referring to the wafer surface), stepped  $E$ -plane bends at the switching junctions, and stepless  $E$ -plane input/output port transitions. The fabricated devices have axially aligned standard WR-3.4 waveguide interfaces

(864 $\mu\text{m}$  $\times$ 432 $\mu\text{m}$ ) so that the stacked chips can be mounted directly and aligned to standard WR-3.4 flanges with inner alignment holes without needing intermediate transitions. The inner alignment holes, instead of outer ones, are utilized for chip-to-flange alignment due to the significantly smaller size of each device compared to the outer dimension of a standard flange. One alignment hole is tightly fitted with a circular hole, and the other is elliptically fitted to ensure precise and repeatable alignment with the accuracy of  $\pm 5\mu\text{m}$  in the  $x$ - and  $y$ -directions [23], [26].

For electrostatic robustness, the MEMS actuators are designed in a push-pull configuration, i.e., dual-actuator, to reduce the required travel distance of the MEMS-RSs compared to a single actuator system. Therefore, the switching cantilevers are fabricated at a mid-state position ( $g=10\mu\text{m}$ ) in the non-actuated state. This leads to the necessary displacement of  $10\mu\text{m}$  in each direction, instead of  $20\mu\text{m}$ , which is designed to occur at the actuation voltage of 40V. However, the actuators are designed to handle up to  $15\mu\text{m}$  of displacement to enhance the actuator's robustness against fabrication tolerances. Fig. 3 shows a scanning electron microscope (SEM) image of a MEMS-RS controlled by the push-pull MEMS actuators. The actuating mechanism consists of four comb drive sections on each side, in which every section consists of fifty interdigitated comb fingers, and the restoring/suspension mechanism includes eight parallel 1.5-folded cantilever-beam springs [20], [27], [28]. Besides, the natural resonance frequency of the mass-spring system is calculated numerically, and it is around 3KHz, which is an upper bound for the switching speed. Thus, the switching speed is expected to be in the order of a few hundred microseconds.

Fig. 4 and Fig. 5 show the simulated performance of the double MEMS-RSs SPST switch (solid lines) with different switching cantilever gaps in the ON and OFF states, respectively. It is evident from Fig. 4 that the ON-state  $RL$  ( $|S_{11}|$ ) exhibits a dependency, while the  $IL$  ( $|S_{21}|$ ) remains relatively constant by varying the gap. Besides, according to Fig. 5, even though the OFF-state isolation ( $|S_{21}|$ ) depends strongly on the gap between the switching cantilevers at the contact area, the  $RL$  ( $|S_{11}|$ ) does not exhibit significant variations and, as expected, a larger contact gap deteriorates the OFF-state isolation. The switch operates even in capacitive contact mode with isolation of better than 32 dB and 29 dB if the contact gap remains below 250nm and 300nm, respectively. Furthermore, the simulated performance of the single MEMS-RS switch (dashed lines) in the ON and OFF states is also depicted in Fig. 4 and Fig. 5, respectively. As can be observed, the ON-state  $S$ -parameters are stable (both  $|S_{11}|$  and  $|S_{21}|$ ) against the gap variation, while the OFF-state  $S$ -parameters depend strongly on the contact gap. According to Fig. 5, the OFF-state isolation of the double MEMS-RSs switch is more than doubled compared to the single MEMS-RS switch at the same contact gap.

Fig. 6 shows the influence of the switching cantilever's width on the ON-state  $IL$  and  $RL$  (when  $g = 20\mu\text{m}$ ) and OFF-state  $ISO$  (when  $g = 300\text{nm}$ ). A thinner cantilever slightly improves the ON-state  $RL$  at the cost of decreasing the

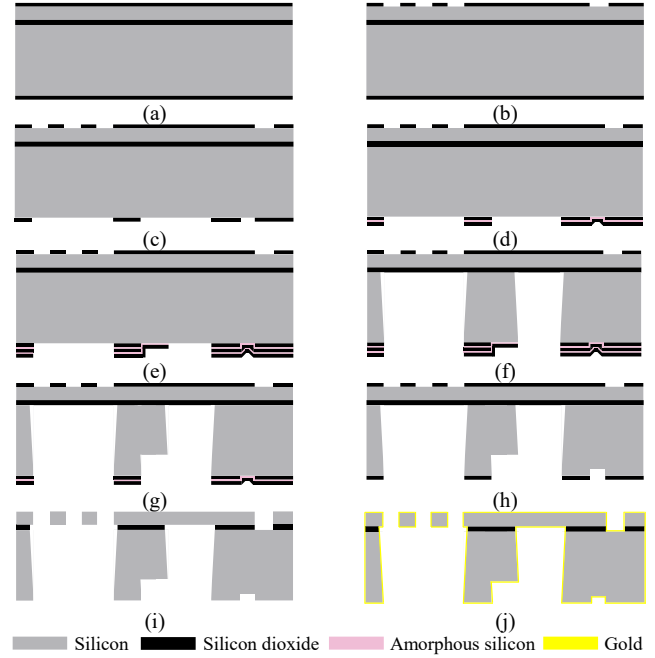


Fig. 8. Step-by-step illustration of the fabrication process flow. (a) SOI wafer; (b) device layer hard-mask lithography; (c) first handle layer hard-mask lithography; (d) second handle layer hard-mask lithography; (e) third handle layer hard-mask lithography; (f) full-height handle layer silicon etching, 275 $\mu\text{m}$ ; (g) etching of the  $E$ -plane steps inside the waveguides in the handle layer, 106 $\mu\text{m}$ ; (h) shallow silicon etching (clearance area) on the handle layer to avoid short-circuiting and stiction, 6 $\mu\text{m}$ ; (i) device layer silicon etching, 30 $\mu\text{m}$ , and buried oxide removal to release the MEMS structures (j) gold sputtering.

operation bandwidth and has a negligible effect on the ON-state  $IL$  and OFF-state  $ISO$ . Therefore, the cantilever's width is chosen to be  $5\mu\text{m}$  as a compromise between the performance, mechanical reliability, and fabrication robustness.

As stated before, the fabrication process only allows the implementation of stepped geometries with the step toward the device layer of the SOI wafer. Therefore, to facilitate characterization, the reduced-height in-plane waveguides (275 $\mu\text{m}$ -height), which are defined by the handle layer, are routed to the top and the bottom surface of the device with stepless  $E$ -plane transitions to standard WR-3.4 waveguide interfaces (864 $\mu\text{m}$  $\times$ 432 $\mu\text{m}$ ). Fig. 7 shows the simulated performance along with an overview and detailed dimensions of the designed transition, indicating the simulated  $IL$  and  $RL$  are better than 0.15 dB and 17 dB in the 220-290 GHz frequency band, respectively.

### III. FABRICATION AND ASSEMBLY

All the chips are processed simultaneously on the same 4-inch silicon-on-insulator (SOI) wafer, and all the features are etched in the silicon substrate by deep-reactive-ion-etching (DRIE) process. Fig. 8a-j outlines the fabrication process flow in detail. Three silicon dioxide ( $\text{SiO}_2$ ) hard-masks for the handle layer and one for the device layer are utilized for the silicon etching. Starting from an SOI wafer, first, the device and handle layers hard-masks are processed and patterned by photolithography and oxide dry etching. Front-to-back and

> REPLACE THIS LINE WITH YOUR MANUSCRIPT ID NUMBER (DOUBLE-CLICK HERE TO EDIT) <

front-to-front mask alignment is checked under microscope and is better than  $\pm 1\mu\text{m}$  in both x- and y-directions.

After processing all the oxide masks, the handle layer is etched all the way down ( $275\mu\text{m}$ ) to the buried oxide layer using the third handle layer hard-mask. Next, the  $E$ -plane steps inside the waveguides are etched, utilizing the second handle layer hard-mask. The etching of the steps has been optimized experimentally to achieve the desired etch depth of  $106\mu\text{m}$ . Then, using the first handle layer hard-mask, a shallow clearance area ( $6\mu\text{m}$ ) is etched above the DC voltage lines and suspended structures to avoid short-circuiting the voltage lines and stiction of the moving parts. Once the handle layer is processed completely, the microelectromechanically reconfigurable switching surfaces (MEMS-RSs) and electrostatic actuators are etched in the device layer and released by removing the buried oxide layer using vapor HF. Besides, the vapor HF etches the buried oxide layer isotopically and isolates the voltage pads from the rest of the chip's area, which is the switch's ground pad, by etching the oxide underneath them. Afterward, a thin layer of gold,  $200\text{nm}$  on the device and  $1500\text{nm}$  on the handle layer, is sputtered on the chips, ensuring that the deposited gold is more than the penetration depth at the designed frequency range of  $220\text{--}290\text{GHz}$ , to avoid increasing the insertion loss. In fact, the gold thickness is optimized experimentally not to cover the surfaces underneath the DC pads that are not directly exposed; thus, the voltage pads remain isolated to avoid high leakage current or even short-circuiting the electrostatic MEMS actuators.

Finally, the chips are aligned by a vernier scale (shown in Fig. 9b) patterned on four corners of the chips [21], [29] and bonded by thermo-compression bonding at  $200^\circ\text{C}$ .

Fig. 9a shows an optical microscope picture of the fabricated metalized chips before and after bonding. As can be seen, the top and bottom chips (chips #1 and #4) are intentionally smaller, facilitating easy access to the DC voltage pads on chips #2 and #3. Furthermore, Fig. 9b shows a zoomed-in picture of only chip #2, along with two scanning electron microscope (SEM) images, depicting the electrostatic MEMS actuator and the vernier scale utilized for chip-to-chip alignment. Moreover, Fig. 10a-c shows three SEM images from the reduced-height in-plane waveguide etched in the handle layer, the stepped  $E$ -plane bend at the switching junction with a cross-section view of the step, and the MEMS-RS with zoomed-in views of the switching cantilevers, respectively. The patterns visible at the bottom of the waveguide in Fig. 10a-b are  $6\mu\text{m}\times 6\mu\text{m}$  etch holes used to release a dummy fall-out structure placed inside the waveguides to protect the profile of the sidewalls. These etch holes, which are demonstrated in detail in [30], have no considerable effect on the RF performance of the switch. The shallow clearance area above the suspended structures is also visible in Fig. 10a-b, and the debris in the cross-section image in Fig. 10b is due to the dicing process.

#### IV. CHARACTERIZATION AND ANALYSIS

Table 1 shows the measured displacement of the microelectromechanically reconfigurable switching surface (MEMS-RS) versus the applied actuation voltage in both

Table 1. MEMS-RSs displacement versus applied voltage in the blocking (OFF) and propagating (ON) states.

Voltage (V)	blocking state displacement ( $\mu\text{m}$ )	Propagating state displacement ( $\mu\text{m}$ )
00.0	0.0	0.0
37.0	7.5	7.5
38.0	8.2	8.2
39.0	9.0	9.0
40.0	9.5	9.5
41.0	10.0	10.2
42.0	10.0*	11.0
43.0	10.0*	11.8
44.0	10.0*	12.5
45.0	10.0*	13.5
46.0	10.0*	14.2
47.0	10.0*	15.0
48.0	10.0*	15.0**

\* The cantilevers are in contact, and further increasing the applied voltage only reduces the contact gap, which is not visible even under microscope.  
\*\* The stoppers prevent further displacement of the actuator.

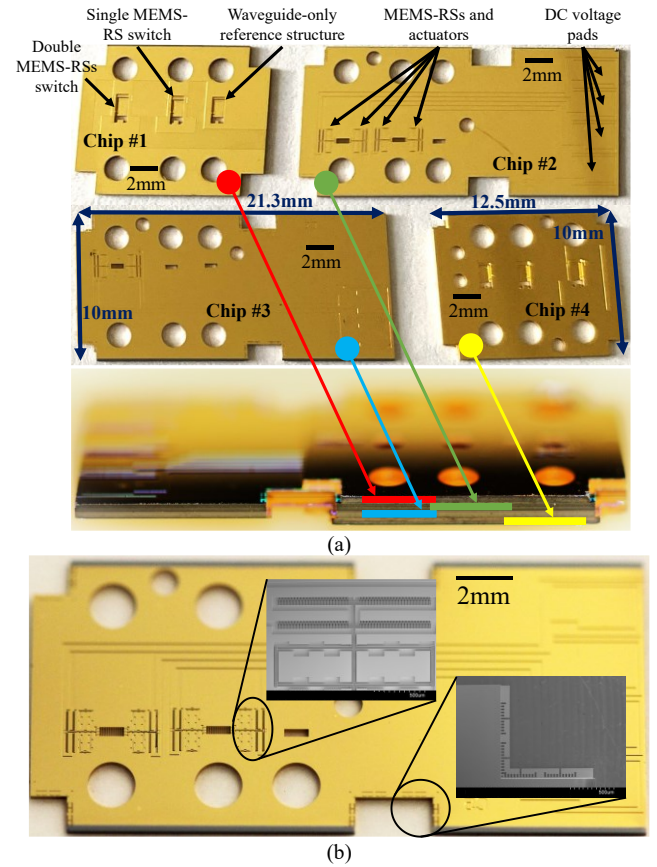


Fig. 9. (a) Optical microscope pictures of the fabricated chips before and after thermo-compression bonding; (b) zoomed-in picture of chip #2 with two scanning electron microscope images showing the electrostatic actuator and the vernier scale used for chip-to-chip alignment.

blocking (OFF) and propagating (ON) states. The MEMS-RS reaches  $10\mu\text{m}$  of displacement at  $41\text{V}$ , at which, in the OFF state, the switching cantilevers are either in contact or in close proximity (capacitive contact mode). Further increasing the applied voltage increases the electrostatic force and reduces the contact gap; therefore, the OFF-state  $S$ -parameters are measured up to  $50\text{V}$ . In addition, the displacement of the MEMS-RS is measured and recorded up to  $15\mu\text{m}$  in the ON state, the point at which the stoppers prevent further displacement of the MEMS-RS.

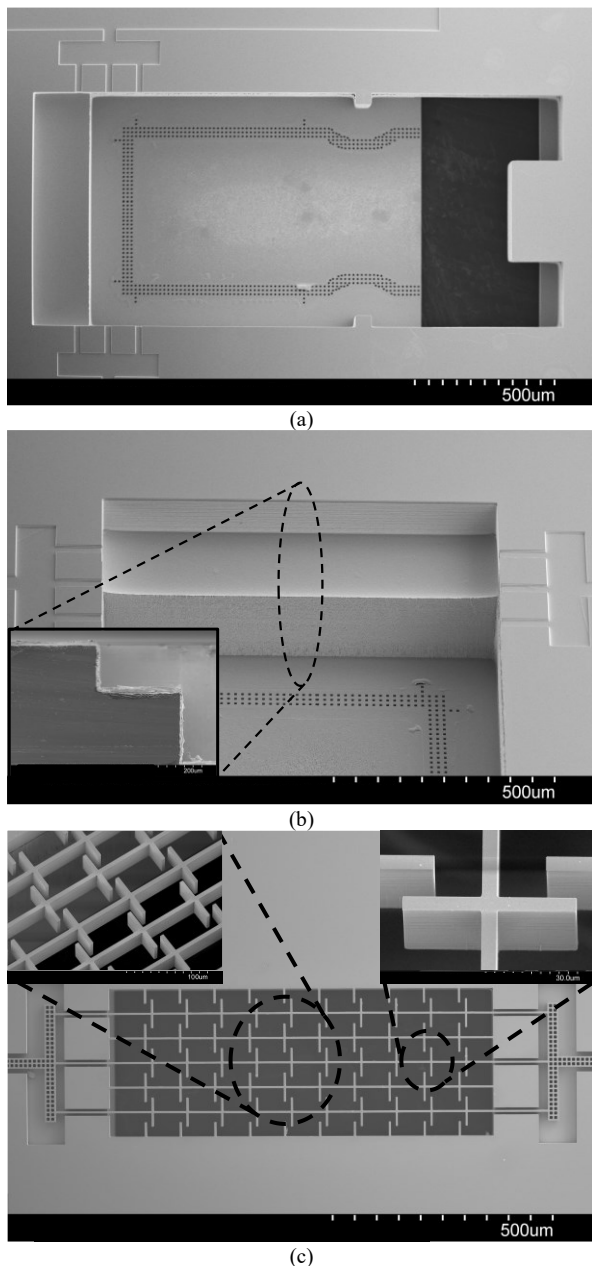


Fig. 10. Scanning electron microscope (SEM) images showing (a) the in-plane waveguide etched in the handle layer; (b) a zoomed-in view of the stepped  $E$ -plane bend at the switching junction, along with a cross-section view of the metalized step; (c) a non-actuated microelectromechanically reconfigurable switching surface positioned in the mid-state with a zoomed-in view on the switching cantilevers.

The RF measurements are carried out by a Rohde & Schwarz ZVA-24 VNA with a pair of ZC330 frequency extenders. The input/output ports of the fabricated devices are located axially so that they can be mounted directly between two standard WR-3.4 test port adapters. Fig. 11 shows the configuration of the measurement setup, in which the stacked device is aligned to the standard flanges utilizing the inner alignment pins. The required actuation voltages can be applied to the DC voltage pads with needles mounted on DC probe positioners or with wires connected to the DC pads by wire bonding or soldering. As can be seen in Fig. 11, the actuation

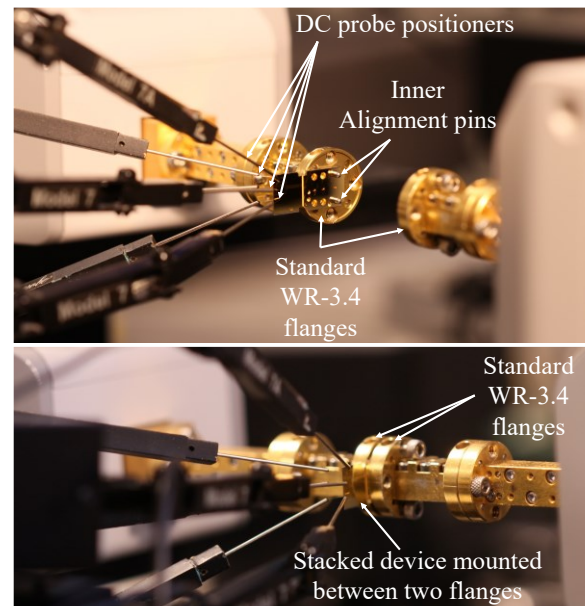


Fig. 11. Configuration of the measurement setup with the stacked device mounted directly on standard WR-3.4 waveguide flanges and actuated with five needles mounted on DC probe positioners.

voltages are applied with five micro-sized semiconductor probe positioners and probe needles due to their fine tips, allowing for accurate positioning and controlled contact with the measurement pads. Moreover, the reference planes are shifted to the test port adapters, i.e., at the surface of the chips, using a standard calibration kit by the TOSM (Thru-Offset-Short-Match) calibration method.

The OFF-state isolation ( $ISO$ ) of the double MEMS-RSs SPST switch is measured at different applied voltages (solid lines) and compared to the simulation data (dashed lines) in Fig. 12a. As can be observed, the measured  $ISO$  is between 28.5-32.5 dB and is relatively uniform in the 200-290 GHz frequency band. Mapping the measured results to the simulation data indicates that the average effective contact gap between the switching cantilevers is between 250-300nm for the fabricated device. Furthermore, according to Fig. 12b, the measured OFF-state  $ISO$  of the single MEMS-RS SPST switch is between 11.5-17.5 dB in the 200-290 GHz frequency band, corresponding to 200-250nm of average effective contact gap in the simulations. Comparing the measured data of the single and double MEMS-RSs switches shows that the  $ISO$  has improved by at least 15.5 dB, which is a direct consequence of introducing an extra MEMS-RS to the single MEMS-RS switch.

In addition, the  $ISO$  of the double MEMS-RSs switch is measured in the states where only one of the MEMS-RSs is in the OFF state and the other is in the ON state, as shown in Fig. 13. As can be seen, the  $ISO$  is better when only MEMS-RS #1 is closed, compared to only MEMS-RS #2 being closed, which is primarily caused by the fabrication tolerances, which are leading to different effective contact gaps. Fitting the measured results to the simulated data implies that the effective contact gap is 200-250nm for MEMS-RS #1 and 250-300nm for MEMS-RS #2, both clearly within the design Consideration (300nm).

> REPLACE THIS LINE WITH YOUR MANUSCRIPT ID NUMBER (DOUBLE-CLICK HERE TO EDIT) <

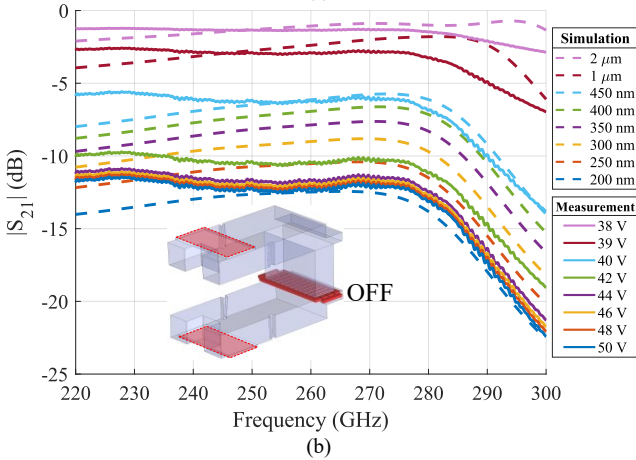
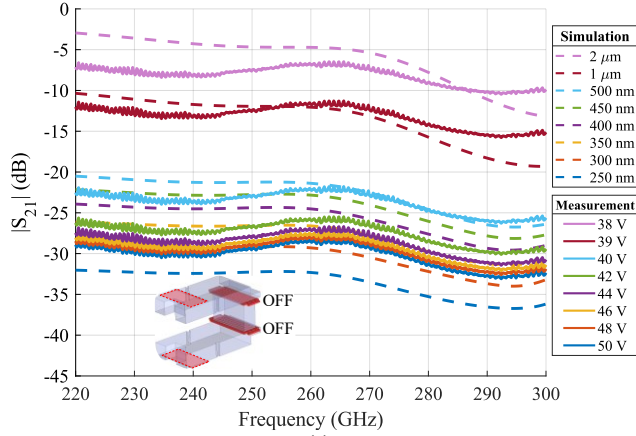


Fig. 12. Measured (solid lines) and simulated (dashed lines) OFF-state isolation of the (a) double MEMS-RSs and (b) single MEMS-RS SPST switches. The simulated data are shown for different contact gaps between the switching cantilevers, and the measured results are shown for different applied voltages.

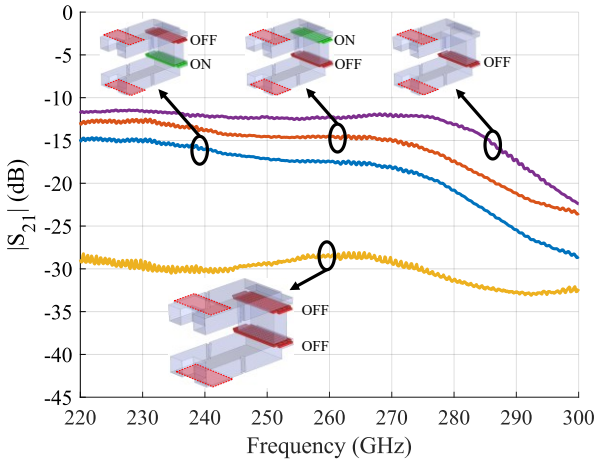


Fig. 13. Measured isolation of the double MEMS-RSs switch when only one of the MEMS-RSs is in the OFF (closed) state, and the other is in the ON (open) state, compared to the measured OFF-state isolation of the single and double MEMS-RSs switches.

Moreover, the measured and simulated OFF-state return loss ( $RL$ ) of the single and double MEMS-RSs switches are shown in Fig. 14, indicating an excellent agreement between the measured results and simulated data. The measured results are associated with the actuation voltage of 50V for both

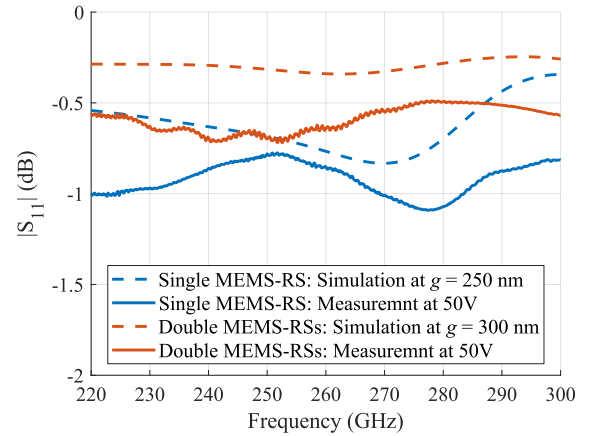


Fig. 14. Measured (solid lines) and simulated (dashed lines) OFF-state return loss of the single and double MEMS-RSs switches.

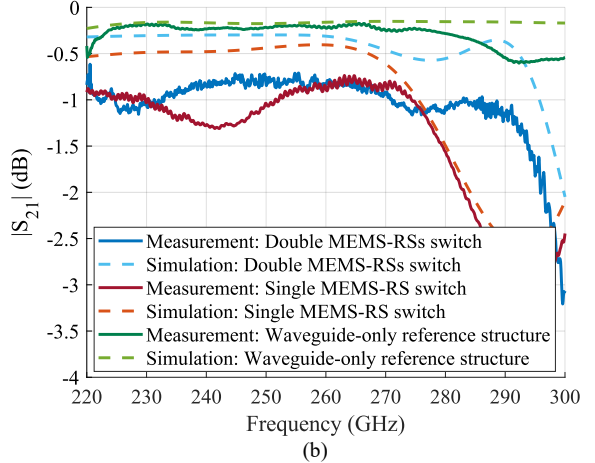
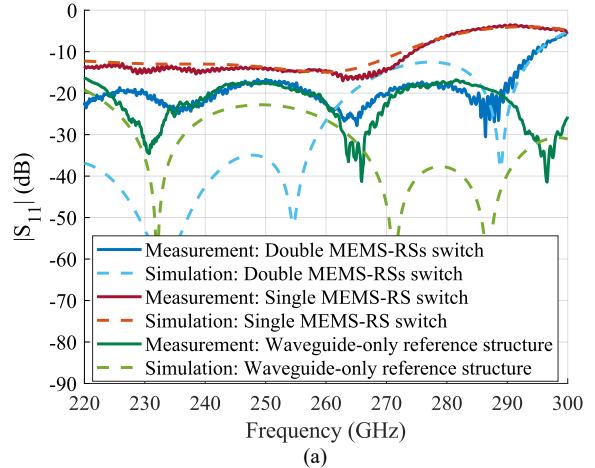


Fig. 15. Measured (solid lines) and simulated (dashed lines) ON-state (a) return loss and (b) insertion loss of the double MEMS-RSs switch compared to the single MEMS-RS switch and waveguide-only reference structure. The measured results are associated with the actuation voltage of 42V, and the simulated data are shown for the contact gap of 20 $\mu$ m for both switches.

switches, and the simulated data are shown for the contact gap of 250nm and 300nm for the single and double MEMS-RSs switches, respectively. As can be seen, both measured and simulated OFF-state  $RL$  of the double MEMS-RSs switch is better than the single one, which is mainly because of the superior OFF-state  $ISO$  (shown in Fig. 13) of the double MEMS-RSs design.

> REPLACE THIS LINE WITH YOUR MANUSCRIPT ID NUMBER (DOUBLE-CLICK HERE TO EDIT) <

Table 2. Summarized measured performance of the presented double MEMS-RSs single-pole-single-throw (SPST) waveguide switch in this paper, compared with other state-of-the-art waveguide switches operating in the millimeter-wave and sub-THz frequency ranges.

Reference	Frequency (GHz)	Technology	Return loss (dB)	Insertion loss (dB)	Isolation (dB)
[10]	250-310	SPDT Piezo-motor waveguide switch	>20	>0.6	>75
[12]	500-750	SPST MEMS waveguide switch	>20	3-4	>20
[14]	500-750	SPST MEMS waveguide switch	>6*	2.5-3	19-24
[15]	500-750	SPDT MEMS rotating waveguide switch	-	>3	>20
[17]	430-500	SPDT MEMS waveguide switch	>23	>1	>23
[18]	360-500	SPST MEMS waveguide switch	>6*	>6*	>25
[19]	60-75	SPST Monolithic MEMS waveguide switch	>12*	>0.2	>22
[31]	240-320	SPST RF MEMS waveguide switch	>13*	>3.5	>16
[32]	500-750	SPST RF MEMS waveguide switch	>12	0.7-2.7	>17
<b>This work</b>	<b>220-290</b>	<b>SPST MEMS waveguide switch</b>	<b>&gt;17</b>	<b>0.7-1.2</b>	<b>28.5-32.5</b>

\* Not explicitly mentioned in the text and derived from the graphs in the paper.

The improving effect of the interference between the MEMS-RSs is also evident in Fig. 15, which compares the measured and simulated ON-state performance of the single and double MEMS-RSs switches and the waveguide-only reference structure. The measured results are associated with the actuation voltage of 42V, and the simulated data are shown for the contact gap of 20 $\mu$ m for both switches. According to Fig. 15a, the measured return loss (*RL*) of the double MEMS-RSs switch is better than 17 dB at 220-290 GHz (27.5% fractional bandwidth), and the measured *RL* of the single MEMS-RS switch is better than 12 dB at 220-274 GHz (21.8% fractional bandwidth), both in excellent agreement with the simulated data. The visible resonances in the *RL* of the double MEMS-RSs switch are due to the interference between the MEMS-RSs and the formation of a cavity between two such surfaces.

In addition, Fig. 15b shows the measured and simulated ON-state insertion loss (*IL*) of the single and double MEMS-RSs switches and the waveguide-only reference structure. The *IL* of the double MEMS-RSs switch is between 0.7-1.2 dB at 220-290 GHz, and the *IL* of the single MEMS-RS switch and the waveguide-only reference structure are between 0.8-1.3 dB at 220-274 GHz and between 0.2-0.5 dB at 200-290 GHz, respectively. As can be observed, the measured and simulated ON-state *IL* of the double MEMS-RSs switch is better than the single one, which is due to the better ON-state *RL* of this structure. Besides, by comparing the measured *IL* of the double MEMS-RSs switch with the waveguide-only reference structure, it can be concluded that 0.5-0.8 dB of the *IL* is caused by introducing the MEMS-RSs into the waveguide, and the remaining is related to the micromachined waveguides. Although the measured results and the simulation data both follow the same profile, the slight discrepancy between them can be explained by considering the simulated data shown in Fig. 4, Fig. 5, and Fig. 6 and comparing them to the measured results shown in Fig. 12, Fig. 14, and Fig. 15. This discrepancy is mainly due to the fabrication tolerances such as silicon underetching [33] and mask shrinking [23] which lead to thinner switching cantilevers and errors in the electrical contact between the switching cantilevers.

According to measured results, utilizing two MEMS-RSs instead of one and tuning the interference between them by integrated MEMS actuators enhances the operation bandwidth from 54 GHz to 70 GHz and improves all three essential

criteria of SPST switches, i.e., ISO, RL, and IL. Due to its excellent performance, The SPST switch can be used in different signal chains such as radars, imaging, medical devices, and telecommunication systems for signal routing and antenna beam shape switching. It also can be utilized to design more sophisticated switching circuits such as SPDT and crossover switches. Table 2 compares the performance of the presented double MEMS-RSs switch with other waveguide switches operating at the millimeter-wave and sub-THz frequency ranges. According to Table 2, the presented SPST switch in this paper outperforms other state-of-the-art SPST waveguide switches operating in the same frequency band in terms of isolation, insertion loss, return loss, and operation bandwidth.

## V. CONCLUSION

A novel single-pole-single-throw switch based on silicon-micromachined waveguides and MEMS technology is presented in this paper. The switching mechanism operates based on short-circuiting the dominant mode of the rectangular waveguide by two microelectromechanically reconfigurable switching surfaces (MEMS-RSs), in which excellent RF performance has been achieved by tuning the interference between two such MEMS-RSs utilizing integrated electrostatic comb-drive MEMS actuators. The measured blocking (OFF) state isolation of the fabricated SPST switch is between 28.5-32.5 dB and is relatively uniform over the 220-290 GHz frequency band. The propagating (ON) state insertion and return losses, measured between two standard waveguide flanges and including all internal waveguides and port interfaces, are 0.7-1.2 dB and better than 17 dB at the same frequency band, respectively. The measured results were in excellent agreement, with the simulation data with the measured fractional bandwidth of 27.5%, which is almost equal to a full waveguide-band performance.

## REFERENCES

- [1] K. M. K. H. Leong *et al.*, "WR1.5 Silicon Micromachined Waveguide Components and Active Circuit Integration Methodology," *IEEE Trans. Microw. Theory Tech.*, vol. 60, no. 4, pp. 998-1005, 2012, doi: 10.1109/TMTT.2012.2184296.
- [2] B. Beuerle, J. Campion, U. Shah, and J. Oberhammer, "A Very Low Loss 220-325 GHz Silicon Micromachined Waveguide Technology," *IEEE Trans. Terahertz Sci. Technol.*, vol. 8, no. 2, pp. 248-250, 2018, doi: 10.1109/TTHZ.2018.2791841.
- [3] C. Jung-Kubiak *et al.*, "A Multistep DRIE Process for Complex

> REPLACE THIS LINE WITH YOUR MANUSCRIPT ID NUMBER (DOUBLE-CLICK HERE TO EDIT) <

- Terahertz Waveguide Components,” *IEEE Trans. Terahertz Sci. Technol.*, vol. 6, no. 5, pp. 690–695, 2016, doi: 10.1109/TTHZ.2016.2593793.
- [4] T. J. Reck, C. Jung-Kubiak, J. Gill, and G. Chattopadhyay, “Measurement of silicon micromachined waveguide components at 500–750 GHz,” *IEEE Trans. Terahertz Sci. Technol.*, vol. 4, no. 1, pp. 33–38, 2014, doi: 10.1109/TTHZ.2013.2282534.
- [5] F. Boussaha, J. Kawamura, J. Stern, and C. Jung-Kubiak, “2.7 THz balanced waveguide HEB mixer,” *IEEE Trans. Terahertz Sci. Technol.*, vol. 4, no. 5, pp. 545–551, 2014, doi: 10.1109/TTHZ.2014.2342507.
- [6] S. C. Wei, C. H. Yang, Y. C. Chen, T. A. Chen, and C. Y. Chang, “V- And W-Band Substrate Integrated Waveguide (SIW) Mechanical Switch,” *IEEE Trans. Microw. Theory Tech.*, vol. 66, no. 6, pp. 3090–3098, 2018, doi: 10.1109/TMTT.2018.2825381.
- [7] J. Tayebpour, B. Ahmadi, M. Fallahzadeh, O. Shekoofa, and A. Torabi, “A waveguide switch based on contactless gap waveguide technology,” *IEEE Microw. Wirel. Components Lett.*, vol. 29, no. 12, pp. 771–774, 2019, doi: 10.1109/LMWC.2019.2950164.
- [8] J. Sobolewski and Y. Yashchyshyn, “State of the Art Sub-Terahertz Switching Solutions,” *IEEE Access*, vol. 10, pp. 12983–12999, 2022, doi: 10.1109/ACCESS.2022.3147019.
- [9] T. Kawamura and S. Mattori, “Proposal of over 100-GHz band waveguide switch,” *IEEE Trans. Fundam. Mater. (English Transl. Denki Gakkai Ronbunshi)*, vol. 138, no. 5, pp. 210–216, 2018, doi: 10.1002/ej.23136.
- [10] S. Van Berkel, S. Rahiminejad, R. Lin, and G. Chattopadhyay, “A 250–310 GHz Piezo-Motor Actuated SPDT Waveguide Switch With High Isolation,” *IEEE Trans. Terahertz Sci. Technol.*, vol. 13, no. 2, pp. 158–166, 2023, doi: 10.1109/TTHZ.2022.3221303.
- [11] Z. Baghchehsaraei, U. Shah, J. Aberg, G. Stemme, and J. Oberhammer, “MEMS reconfigurable millimeter-wave surface for V-band rectangular-waveguide switch,” *Int. J. Microw. Wirel. Technol.*, vol. 5, no. 3, pp. 341–349, 2013, doi: 10.1017/S1759078713000378.
- [12] T. Reck, C. Jung-Kubiak, and G. Chattopadhyay, “A 700-GHz MEMS Waveguide Switch,” *IEEE Trans. Terahertz Sci. Technol.*, vol. 6, no. 4, pp. 641–643, 2016, doi: 10.1109/TTHZ.2016.2574304.
- [13] M. Daneshmand, R. R. Mansour, and N. Sarkar, “RF MEMS waveguide switch,” *IEEE MTT-S Int. Microw. Symp. Dig.*, vol. 2, no. 12, pp. 589–592, 2004, doi: 10.1109/mwsym.2004.1336050.
- [14] U. Shah *et al.*, “A 500–750 GHz RF MEMS Waveguide Switch,” *IEEE Trans. Terahertz Sci. Technol.*, vol. 7, no. 3, pp. 326–334, 2017, doi: 10.1109/TTHZ.2017.2670259.
- [15] S. Rahiminejad, S. Van Berkel, R. H. Lin, C. Jung-Kubiak, G. Chattopadhyay, and M. Rais-Zadeh, “A MemS Contactless Rotating Terahertz Waveguide Switch,” *IEEE Symp. Mass Storage Syst. Technol.*, vol. 2022-Janua, no. January, pp. 223–226, 2022, doi: 10.1109/MEMS51670.2022.9699786.
- [16] M. Daneshmand and R. R. Mansour, “RF MEMS satellite switch matrices,” *IEEE Microw. Mag.*, vol. 12, no. 5, pp. 92–109, 2011, doi: 10.1109/MMM.2011.941417.
- [17] T. Reck, C. Jung-Kubiak, and G. Chattopadhyay, “A 460 GHz MEMS-Based Single-Pole Double-Throw Waveguide Switch,” *IEEE MTT-S Int. Microw. Symp. Dig.*, vol. 2018-June, pp. 773–775, 2018, doi: 10.1109/MWSYM.2018.8439196.
- [18] D. Laemmler, H. F. Schlaak, C. Weickmann, and R. Jakoby, “Proof of concept for a WR-2.2 MEMS waveguide switch,” in *International Conference on Infrared, Millimeter, and Terahertz Waves, IRMMW-THz*, 2016, vol. 2016-Novem. doi: 10.1109/IRMMW-THz.2016.7758655.
- [19] N. Vahabisani and M. Daneshmand, “Monolithic millimeter-wave MEMS waveguide switch,” *IEEE Trans. Microw. Theory Tech.*, vol. 63, no. 2, pp. 340–351, 2015, doi: 10.1109/TMTT.2014.2378253.
- [20] X. Zhao, U. Shah, O. Glubokov, and J. Oberhammer, “Micromachined Subterahertz Waveguide-Integrated Phase Shifter Utilizing Supermode Propagation,” *IEEE Trans. Microw. Theory Tech.*, vol. 69, no. 7, pp. 3219–3227, 2021, doi: 10.1109/TMTT.2021.3076079.
- [21] A. Gomez-torrent, U. Shah, and J. Oberhammer, “Compact Silicon-Micromachined Wideband 220–330-GHz Turnstile Orthomode Transducer,” *IEEE Trans. Terahertz Sci. Technol.*, vol. 9, no. 1, pp. 38–46, 2019, doi: 10.1109/TTHZ.2018.2882745.
- [22] A. Gomez-Torrent *et al.*, “A Low-Profile and High-Gain Frequency Beam Steering Subterahertz Antenna Enabled by Silicon Micromachining,” *IEEE Trans. Antennas Propag.*, vol. 68, no. 2, pp. 672–682, 2020, doi: 10.1109/TAP.2019.2943328.
- [23] O. Glubokov, X. Zhao, J. Campion, B. Beuerle, U. Shah, and J. Oberhammer, “Investigation of Fabrication Accuracy and Repeatability of High-Q Silicon-Micromachined Narrowband Sub-THz Waveguide Filters,” *IEEE Trans. Microw. Theory Tech.*, vol. 67, no. 9, pp. 3696–3706, 2019, doi: 10.1109/tmtt.2019.2926244.
- [24] Z. Baghchehsaraei, U. Shah, J. Åberg, G. Stemme, and J. Oberhammer, “Millimeter-wave SPST waveguide switch based on reconfigurable MEMS surface,” *IEEE MTT-S Int. Microw. Symp. Dig.*, no. c, pp. 10–13, 2013, doi: 10.1109/MWSYM.2013.6697774.
- [25] A. Karimi, M. M. Gohari, O. Glubokov, U. Shah, and J. Oberhammer, “Full-band Silicon-Micromachined E-plane Waveguide Bend for Flange-to-Chip Connection,” *IEEE Trans. Terahertz Sci. Technol.*, vol. PP, pp. 1–5, 2023, doi: 10.1109/TTHZ.2023.3327587.
- [26] J. Campion, U. Shah, and J. Oberhammer, “Elliptical alignment holes enabling accurate direct assembly of micro-chips to standard waveguide flanges at sub-THz frequencies,” in *2017 IEEE MTT-S International Microwave Symposium (IMS)*, 2017. doi: 10.1109/MWSYM.2017.8058838.
- [27] U. Shah *et al.*, “Submillimeter-Wave 3.3-bit RF MEMS Phase Shifter Integrated in Micromachined Waveguide,” *IEEE Trans. Terahertz Sci. Technol.*, vol. 6, no. 5, pp. 706–715, 2016, doi: 10.1109/TTHZ.2016.2584924.
- [28] H. W. Huang, F. W. Lee, and Y. J. J. Yang, “Design Criteria for a Push-On Push-Off MEMS Bistable Device,” *J. Microelectromechanical Syst.*, vol. 25, no. 5, pp. 900–908, 2016, doi: 10.1109/JMEMS.2016.2574874.
- [29] O. Glubokov, X. Zhao, B. Beuerle, J. Campion, U. Shah, and J. Oberhammer, “Micromachined multilayer bandpass filter at 270 GHz using dual-mode circular cavities,” *IEEE MTT-S Int. Microw. Symp. Dig.*, pp. 1449–1452, 2017, doi: 10.1109/MWSYM.2017.8058894.
- [30] X. Zhao *et al.*, “Silicon micromachined d-band diplexer using releasable filling structure technique,” *IEEE Trans. Microw. Theory Tech.*, vol. 68, no. 8, pp. 3448–3460, 2020, doi: 10.1109/TMTT.2020.3004585.
- [31] N. Zhang, R. Song, J. Liu, and J. Yang, “A Packaged THz Shunt RF MEMS Switch With Low Insertion Loss,” *IEEE Sens. J.*, vol. 21, no. 21, pp. 23829–23837, 2021, doi: 10.1109/JSEN.2021.3113647.
- [32] Y. Feng and N. S. Barker, “High performance 500-750 GHz RF MEMS switch,” *IEEE MTT-S Int. Microw. Symp. Dig.*, pp. 1095–1097, 2017, doi: 10.1109/MWSYM.2017.8058786.
- [33] A. Gomez-Torrent, U. Shah, and J. Oberhammer, “Compact Silicon-Micromachined Wideband 220-330-GHz Turnstile Orthomode Transducer,” *IEEE Trans. Terahertz Sci. Technol.*, vol. 9, no. 1, pp. 38–46, 2019, doi: 10.1109/TTHZ.2018.2882745.



**Armin Karimi** (Student Member, IEEE) was born in Kermanshah, Iran, in 1993. He received his bachelor’s degree in electrical engineering, focusing on Communication Systems, from the University of Tehran in 2016. He received his master’s degree on applied electromagnetics, fields, and waves from the University of Tehran in 2019. Currently, he is a PhD student at the Division of Micro and Nano Systems at KTH Royal Institute of Technology, Sweden.

He is the recipient of the Young Engineer Award at European Microwave Week 2023, Berlin, Germany and the Best Student Paper Award presented at Swedish Microwave Days 2023, Stockholm, Sweden. His research interests are applied

> REPLACE THIS LINE WITH YOUR MANUSCRIPT ID NUMBER (DOUBLE-CLICK HERE TO EDIT) <

electromagnetics, RF-MEMS, Nanofabrication, Microwave and mm-wave active and passive components, array antenna, filter, imaging systems, metamaterial and metasurface, and signal chain design.



**Umer Shah** (S'09-M'14) was born in 1981 in Pakistan. He received his BS degree in Engineering from GIK Institute Pakistan in 2003, Master of Science degree in Wireless Engineering from the Technical University of Denmark (DTU) in 2007 and PhD degree in Microsystem Technology from KTH Royal Institute of Technology, Stockholm, Sweden in 2014. Since May 2014, he is a Postdoctoral researcher in the Micro and Nano systems group at KTH Royal Institute of Technology. His research focuses includes RF MEMS based filters, phase shifters, matching circuits and antennas.

Umer has authored and co-authored more than 30 reviewed research papers. He is the recipient of the Best Student Paper Award presented at Asia Pacific Microwave Conference 2010, Yokohama, Japan. Umer is also the recipient of the "2014 IEEE MTT Graduate Fellowship Award" for his research activities.



**Suxian Yu** (Student Member, IEEE) was born in Jilin, China, in 1992. She received the B.Sc. and M.Sc. degrees in mechanical and electrical engineering from the Beijing Institute of Technology, Beijing, China, in 2013 and 2016, respectively. She is currently pursuing the Ph.D. degree at the KTH Royal Institute of Technology, Stockholm, Sweden. Her current research interest is millimeter and submillimeter calibration switch circuits for space applications.



**Joachim Oberhammer** (M'06-SM'12), was born in Brunico, Italy, in 1976. He received the M.Sc. degree in electrical engineering from the Graz University of Technology, Graz, Austria, in 2000 and the Ph.D. degree from the KTH Royal Institute of Technology, Stockholm, Sweden, in 2004.

He was a Post-Doctoral Research Fellow with Nanyang Technological University, Singapore, in 2004 and with Kyoto University, Kyoto, Japan, in 2008. He was leading radio frequency/microwave/terahertz (THz) microelectromechanical systems research at

KTH Royal Institute of Technology till 2010, was an Associate Professor till 2015, and now working as a professor in microwave and THz microsystems. He was a Guest Researcher with Nanyang Technological University, in 2007 and NASA Jet Propulsion Laboratory, Pasadena, CA, USA, in 2014. He has authored or coauthored more than 100 reviewed research articles. He holds four patents. Dr. Oberhammer served as a TPRC member of IEEE Transducers 2009 and 2015, the IEEE International Microwave Symposiums 2010–2016, IEEE Micro Electromechanical Systems 2011 and 2012, and IEEE Radio and Wireless Week 2015 and 2016. He has been a Steering Group member of the IEEE MTT-S and AP-S Chapters Sweden since 2009. Since 2014, he has been a Steering Group member of the Young Academy of Sweden. He was a recipient of an award by the Ericsson Research Foundation, a grant by the Swedish Innovation Bridge, and a scholarship by the Japanese Society for the Promotion of Science, in 2004, 2007, and 2008, respectively. The research work he is heading received six Best Paper Awards (five of which at IEEE conferences) and four IEEE Graduate Fellowship Awards (by the IEEE MTT-S and by AP-S) since 2009. In 2013, he received an ERC Consolidator Grant by the European Research Council.